



Direct and indirect contact of an austenitic high-temperature alloy to eutectic chloride melts with possible consequences for inhibitor strategies

Downloaded from: <https://research.chalmers.se>, 2023-12-29 09:03 UTC

Citation for the original published paper (version of record):

Mohamedin, E., Pochi, A., Geers, C. (2023). Direct and indirect contact of an austenitic high-temperature alloy to eutectic chloride melts with possible consequences for inhibitor strategies. *Engineering Failure Analysis*, 150. <http://dx.doi.org/10.1016/j.engfailanal.2023.107332>

N.B. When citing this work, cite the original published paper.



Direct and indirect contact of an austenitic high-temperature alloy to eutectic chloride melts with possible consequences for inhibitor strategies

Esraa Hamdy ^{a,*}, Antoine Pochi ^{b,1}, Christine Geers ^a

^a Department of Chemistry and Chemical Engineering, Chalmers University of Technology, 412 96 Gothenburg Sweden

^b Department of Materials and Sustainable Development, University of Burgundy, Dijon, 21000, France



ARTICLE INFO

Keywords:

Power generation
Steel
High-temperature corrosion
Microscopic characterisation and microanalysis
Molten chlorides
Internal attack

ABSTRACT

There is an inevitable difference between direct and indirect contact of metals with eutectic chloride melts defined by the gas phase impurity content, here, humidity and oxygen in argon. The impurities-to-salt ratio will always be higher in the gas phase allowing for a more aggressive attack on metal components. This effect has been studied on a decommissioned metal container from an experimental high-temperature setup, which has never been in direct contact with a chloride melt but with its evaporated species; the vessel lasted only a short time, 700 h. It was found that the vessel suffered more severe damage when exposed to evaporated salt species than in direct contact with the salt melt; the estimated metal thickness loss per year is higher by almost three-fold than the direct contact. In contrast to 253MA fully immersed in MgCl₂-KCl, magnesium has not been the most-active cationic species causing corrosion in the vessel wall exposed to evaporated salt species; instead, it has been potassium. Consequently, this unexpected observation needs to be carefully considered in the design of a Gen3-CSP storage tank and the applied inhibitor strategy.

1. Introduction

In 2017, the national renewable energy laboratory of the U.S. Department of Energy (NREL) launched a report demonstrating the roadmap for the third generation (Gen3) of concentrated solar power plant (CSP) technology [1]. Gen3 of CSP plants aims at increasing the efficiency of thermal to-electrical conversion in the power block; this requires employing heat transfer fluid (HTF) and thermal energy storage (TES) media that can operate at temperatures higher than 700 °C. The high thermal stability and low cost of molten chlorides, in addition to their desirable thermophysical properties, give them the potential to be employed as HTFs and TES media for next-generation CSP plants. However, molten chlorides are known for their severe corrosivity to metallic components, which brings a serious challenge to their implementation [2,3].

Thermodynamically, impurity-free molten chlorides are not corrosive to most alloy components since they are redox-inactive. Corrosion in a chloride salt environment is known to be impurity-driven corrosion [1,4–6]. The most common impurities are oxygen or moisture that oxidise alloy components and bring them into salt flux in ionic form [1,5,6]. The resulting material loss occurs

* Corresponding author.

E-mail address: esraah@chalmers.se (E. Hamdy).

¹ The author has been an intern at (a) while conducting this study.

rapidly and does not slow down to a lack of passivating oxide scales. Besides alloy components, the chloride melt can also react with oxygen and moisture, producing Cl_2 and HCl [1,6–9].



Different aspects need to be considered to understand the corrosivity of molten chlorides on metallic materials. Ding et al. reviewed the corrosion behaviour of different alloys in contact with chloride melts. In a review study, they classified the corrosion processes caused by a chloride melt into 1) interaction of the salt with the environment/cover gas, 2) reactions within the salt melt, e.g., decomposition or hydrolysis, and 3) interaction of metallic components with the salt melts or salt-containing environment [9]. It was concluded that corrosion by chloride melts has different corrosion mechanisms due to the three main processes mentioned earlier.

The corrosion resistance of alloys differs based on the chemical composition of the alloys. Although Ni-based superalloys have shown superior corrosion behaviour to chloride melts compared to stainless steels [9], no certain conclusion could be drawn regarding the Ni-content since some studies showed failure cases of high Ni% to resist corrosion, as has been published in a review paper by Ding et al. [10].

Furthermore, the significant effect of operating temperature, cover gas employed, and impurities in the melt have been reported. Therefore, efforts are being made to reduce impurities content and implement salt purification methods [5,11–14].

Hygroscopic salts such as MgCl_2 and ZnCl_2 are utilised to lower the melting temperature of the salt mixture. Many studies have been dedicated to investigating their corrosion influence on metals [9,11,12,14,15]. Highly hygroscopic MgCl_2 reacts with water impurities to MgOHCl at a temperature $> 300^\circ\text{C}$ and further to MgO and HCl above 550°C [14]; see equations (3), (4) and (5) [16].



Alloy components can react with moisture adsorbed by salts or by interacting with HCl formed by MgCl_2 hydrolysis or with oxygen which could be dissolved in the salt melts or present as impurities in the gas [14].

Notably, after the “SunShot Initiative” launched by the U.S. Department of Energy, various research studies investigated the corrosivity of chloride melts on iron-based, nickel-based and model alloys at a temperature range of $500\text{--}650^\circ\text{C}$ [2,17–19]. It has been reported that, with the presence of oxygen or moisture, the chloride salts strongly attack every alloy with excessive chromium leaching, preferably along grain boundaries [4,20,21]. Laboratory tests confirmed the presence of defect-rich porous scales, selective element leaching, pore formation in bulk materials and inter-granular attack [2,4,22–24]. Equations (Eq. (6)) and (Eq. (7)) represent two possible reactions causing the destabilisation of a chromia scale at high temperatures. Chromia reacts with potassium chloride in excess oxygen, forming soluble alkali chromate, volatile chromium chloride, and oxy-chloride species [4].



Since the corrosion rate of alloys depends on oxygen and impurities concentration, intensive efforts have been made to reduce them by, e.g., purification [9,11,12,14,15]. A second approach is the dehydration of hydrophilic salts, e.g., $\text{MgCl}_2 \cdot 6 \text{H}_2\text{O}$, by stepwise heating while sweeping volatile side products away with inert gas. This method limits the formation of corrosive species such as MgOHCl . Even though the stepwise heating procedure reduces the corrosivity of the melt, it does not eliminate all hydroxide impurities [9,16,25].

Other inhibitor strategies have been adopted to reduce oxygen concentration and humidity in the melt chemically by adding Mg metal for potassium-magnesium chlorides [15,26–29] or metallic Be in lithium-beryllium fluorides [30].

Kurley et al. proposed carbochlorination as a salt purification method; in this method, various carbochlorinating reagents, e.g., $(\text{C} + \text{Cl}_2)$, $(\text{CO} + \text{Cl}_2)$ and (CCl_4) , are utilised to react with MgCl_2 and even coverage gases used and produce a gaseous side product that can be removed easily from the melt [14]. According to the authors' knowledge, carbochlorination is the only method in literature treating salt and gas impurities.

Few studies were conducted to study the corrosivity of molten chloride at temperatures higher than 650°C and long-term, > 100 h. In addition, most of the studies focused on metal corrosion and purification approached in direct contact with the melt.

In our former publication, we investigated the corrosion resistance of FeCrAl and FeNiCr alloys immersed in 64 wt% KCl-36 wt% MgCl_2 at 800°C under flowing Ar [31]. The specifically built experimental setup was designed to conduct corrosion exposures of samples fully immersed in salt melts under controlled conditions [31–33].

The vessel hosting the experiments has not been in direct contact with the eutectic chloride melt. However, it has been exposed to evaporating salt species and impurities in the flowing argon stream. After only 700 h in operation, this vessel was so heavily corroded that it required decommissioning and replacement. To understand the most critical conditions, we systematically investigated the vessel in a failure case study by metallographic and chemical means. Furthermore, this study was interesting since it allowed the corrosion evaluation along a temperature gradient of $550\text{--}800^\circ\text{C}$.

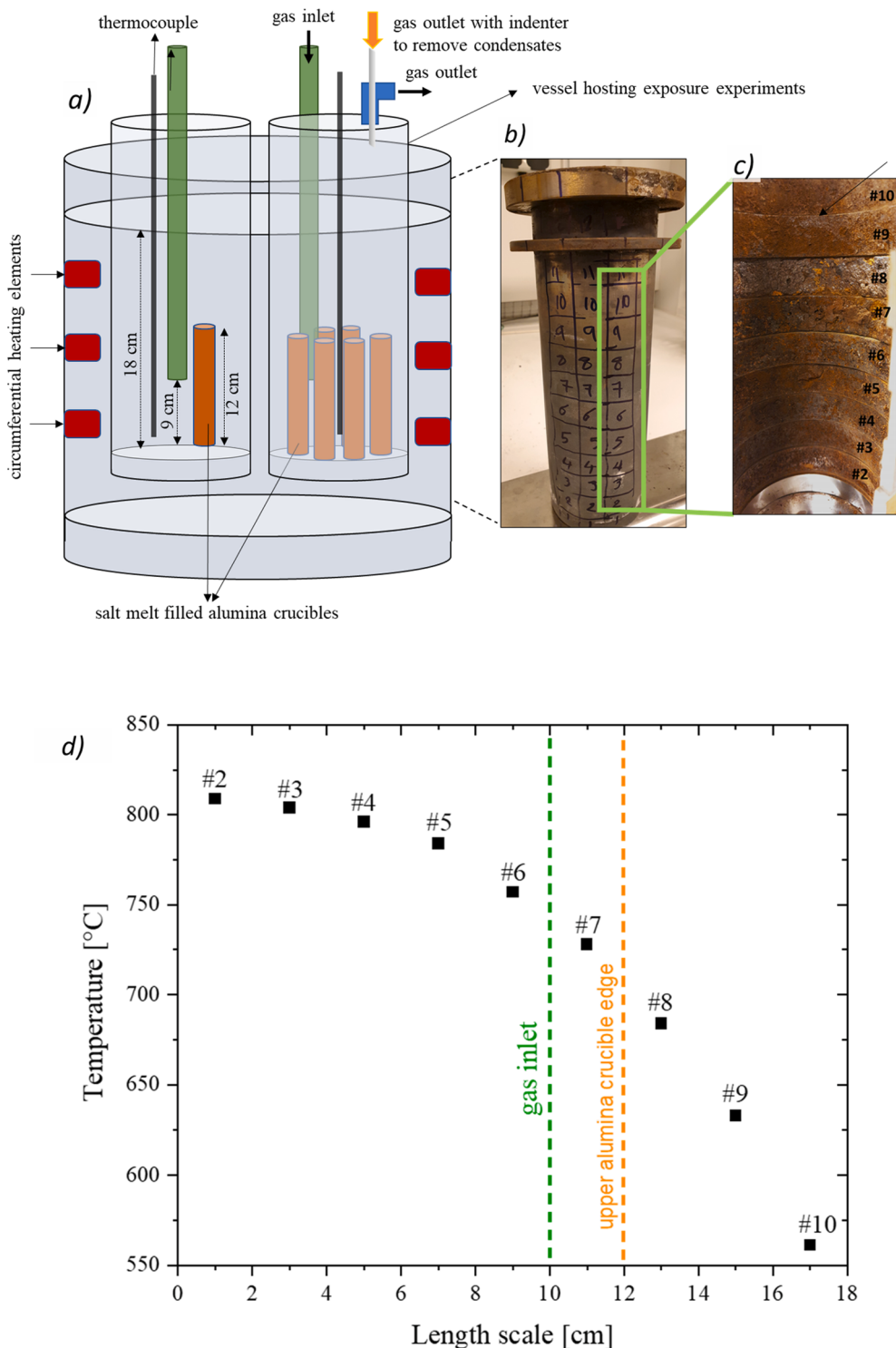


Fig. 1. a) Schematic illustration of the experimental setup showing two vessels hosting six crucibles each. b) vessel before and after partitioning, c) vessel interior was scrubbed before decommissioning and brushed corrosion products were collected for analysis besides cutting the vessel into horizontal rings for investigation. d) Temperature profile along the vessel during operation at 800 °C.

2. Experimental layout

Our former publication used an equivalent experimental setup for an alkali carbonate study at 800 °C [34]. In this work, however, the investigated vessels have been hosting molten chloride exposures, which required an additional purification step. In contrast to the long total exposure time in our carbonate-tested vessels of more than 4000 h, chloride-hosting vessels were only 700 h, with two occasions of vessel venting at 600 °C.

2.1. Experimental setup

The setup designed in this work is equivalent to the experimental setup that has been used for alkali carbonate studies at 800 °C [32,34]. The setup, purchased from Nabertherm (model Top 60), was redesigned by our workshop to host two cylindrical vessels made of the high-temperature alloy 253MA, as shown in the schematic sketch in Fig. 1. The furnace is heated by three heating elements adjusted at three height levels surrounding the vessels. Each vessel is sealed by a lid containing a thermocouple inlet used for calibrating the system, gas inlet, and gas outlet. As shown in Fig. 1, the gas outlet was modified to host an anti-clogging metal rod, regularly punching through condensed salt precipitates without venting the system. A crucible holder was machined to host six long alumina crucibles containing about 10 g of the alkali chloride mixture each.

2.2. Vessel material

A 5 mm thick 253MA austenitic high-temperature alloy was selected as a test material for our prototype setup. The initially measured chemical material composition is shown in the first two rows in Table 1. This alloy is known for its high strengths and high corrosion resistance in air at high temperatures by forming a protective chromia scale supported by silicon and cerium additions [34].

Also in Table 1 are shown the thermodynamically computed phase equilibria of alloy 253MA at 1050 °C and 800 °C [34]. With this, phase changes in the microstructure can be anticipated during the vessel used at 800 °C. At 1050 °C, a common alloy heat treatment temperature during alloy production, 253MA alloy is a nearly single-phase alloy, 99.99% mass% FCC phase. While at 800 °C, the mass fraction of the FCC phase is reduced to 92.14%, and fractions of (Cr,V)₂N, M₂₃C₆, (Cr,Fe)₃P, Ce₂S₃, η-phase and σ-phase precipitates are expected to form.

2.3. Exposures

The setup temperature was calibrated at the lowest point of the crucibles, where sample coupons can be placed in alumina crucibles fully immersed to conduct exposures isothermally at 800 ± 10 °C. The exposures were performed under argon with a 50 ml/min flow rate for each vessel. Oxygen concentration was controlled for each vessel and was found to be constantly in the range of 30–40 ppm after 12 h purging with argon.

The investigated vessels hosted chloride melt exposures; the melt was a binary eutectic mixture consisting of 64 wt% KCl and 36 wt % MgCl₂. Due to the crucial effect of humidity impurities on alloy corrosion behaviours, as reported in numerous publications [5,9,14,35–37], chloride melts require an additional purification step before exposing the samples to 800 °C. A thermal purification process was carried out as follows: the chloride mixture was dried for at least 12 h at 100 °C, another two h at 200 °C and finally two h at 300 °C. Afterwards, the setup was cooled to room temperature, and the samples were placed in the salt-containing crucibles. Later, the vessels are purged for 12 h with argon gas and another 12 h heated to 120 °C. As a final step, the setup is rapidly ramped up to 750 °C and held for one h before starting the exposure at 800 °C to achieve a homogeneous heat distribution in the comparatively large furnace room. The binary eutectic salt used has a melting point of 450 °C.

Furthermore, KCl and MgCl₂ exhibit vapour pressures at 800 °C [38], which cause condensation in the upper, colder regions of the

Table 1

Upper row: Measured alloy composition of 253MA via EDS. Second table part: computed phase equilibrium compositions of alloy 253MA at 1050 °C and 800 °C [34].

Measured Composition of Alloy 253MA (wt%)									
Fe	C	Si	Mn	P	S	Cr	Ni	N	Others
Bal.	~0.08	≤1.97	≤0.55	≤0.02	≤0.16	~20.9	~10.6	≤0.14	Ce; V
TCFE single point calculation considering the nominal alloy composition and for Mn: 0.55%; P: 0.002%; S: 0.0016%									
253MA at 1050 °C									
Phase		Mass fraction [%]		Phase				Mass fraction [%]	
FCC		99.29		FCC				92.14	
(Cr, V) ₂ N		0.61		(Cr, V) ₂ N				0.18	
M ₂₃ C ₆		0.04		M ₂₃ C ₆				1.31	
(Mn,Cr)S		0.02		(Cr,Fe) ₃ P				0.01	
Ce ₂ S ₃		0.04		Ce ₂ S ₃				0.04	
				η-phase				2.65	
				(Cr, Mn)S				0.02	
				σ-phase				3.65	

vessels. A movable metal rod was installed at a T-junction at the gas outlet (see schematic in Fig. 1) to sweep away clogging condensation products regularly. After completion of the experiment, the challenge remained to remove the salt from the coupon while it was still molten to avoid rinsing it with water. Therefore, the furnace vessels are heated to 600 °C, opened, the crucible holder is quickly removed from the vessel, and one by one, samples are poured from its melt and collected for further inspection.

2.4. Lifecycle of the vessel

After approximately 700 h operation at the target temperature, the analysed vessel for this study was decommissioned due to substantial degradation of the interior. Table 2. shows a detailed listing of all process steps and interruptions the investigated vessel went through before decommissioning.

To study the corrosion of the vessel along the temperature gradient, the vessel was cut into fourteen horizontal rings using a water-cooled diamond blade. Each ring was cut into 20 × 20 mm coupons marked with numbers starting with #2 at the vessel bottom and #10 close to the sealing lid. Before vessel cutting, the interior was scrubbed with a stainless-steel lab spatula and brushed corrosion products were collected at each ring. However, it is noteworthy that part of the corrosion products of the decommissioned vessel has been lost due to the following: i) brushing the vessel using a steel wire after each exposure. ii) crucible-holder lifting to pour the molten salts from the crucible and extract the tested coupons.

Fig. 1c depicts the temperature gradient along the vessel wall from 800 ± 10 °C at the bottom until reaching its lowest temperature (560 °C) at the upper section. The temperature difference between the vessel centre and wall due to the exterior heating was insignificant.

2.5. Characterisation techniques

After the vessel was decommissioned and cut into fourteen rings, two coupons were cut from each section ring to be analysed. One was dedicated to cross-section investigations, while the second coupon was used for X-ray diffraction (XRD) analysis.

For the XRD analysis, no sample surface preparation was required. For the cross-section investigation, samples were first sputter-coated with gold, then hot embedded in Bakelite using Struers PolyFast. Last, the cross-section samples were ground and polished with diamond suspension until a mirror-like finish was achieved.

The SEM analysis of the samples was performed using a Phenom ProX Desktop SEM equipped with an EDX detector. The electron beam was operated in backscatter electron mode (BSE) at an accelerating voltage of 15 kV. In addition, the residual metal thickness in each sample was measured using the SEM instrument's light microscope mode. The cross-section samples were also investigated with optical microscopy using a Zeiss Axio Vert.A1. The samples were scanned using the dark mode filter, where some characteristic features could be observed, as discussed in section 3.3 (b).

The XRD surface analysis was performed using Bruker D8 Discover XRD equipped with a Cu source, a secondary Si monochromator, and a point detector.

Table 2
Lifecycle of the investigated vessel.

Process	Operation Conditions		
	Temperature	Duration	Atmosphere
Prior to chloride melt exposure			
Pre-oxidation step (at 900 °C), air	24 h	–	–
Exposures to KCl-MgCl ₂ melt (Ar, 800 °C)			
Experiment no. 1			
Salt purification	110 °C 200 °C 300 °C 750 °C	24 h 2 h 2 h 1 h	Ar
Exposure	800 °C	168 h (paused after 96 h)	
Evaporated salts clogging the gas outlet after 96 h, vessel opening at room temperature, cleaning up the exhaust line, drying procedure			
Exposure	800 °C	168 h (resumed after 96 h)	Ar
Vessel Opening (Pouring the Melt Out)	600 °C	~70 min.	Air
The vessel was cleaned and brushed after the experiment			
Experiment no. 2			
Salt purification	110 °C 200 °C 300 °C 750 °C	24 h 2 h 2 h 1 h	Ar
Exposure	800 °C	336 h (paused after 96 h)	
Vessel Opening at room temperature, refilling crucibles (half-filled) with new dried salts, purging under Ar for 24 h at 110 °C, then salt purification			
Exposure continuation	800 °C	168 h	
Vessel Opening (Pouring the Melt Out)	600 °C	~75 min.	Air

ImageJ software version 1.52a [34] was employed to measure the area fraction percentage of cavities and internal oxidation detected within tested samples via binarisation.

3. Results

Results have been collected along the temperature gradient shown in Fig. 1. The corrosion behaviour along the vessel wall is compared in three ways: i) remaining metal thickness. Since the vessel wall has been brushed and cleaned on different occasions before decommissioning, measuring the remaining metal thickness is a reliable way to determine how much material was lost during exposure. ii) As shown in section 3.1, the corrosion severity differs significantly along the vessel; therefore, the internal attack depth in each sample is considered. iii) cavities formation is among the distinguishable features of corrosion in such an environment, so that area fractions that cavities occupy are reported. Worth mentioning that we cannot use the classical way of evaluating corrosion kinetics using time- and temperature-dependent mass change values due to the preparation procedure of the investigated vessel, as described in section 2.4.

3.1. Overall corrosion evaluation

The effect of evaporated alkali carbonate species on the 253MA vessel has been assessed by remaining metal thickness and internal attack depth measurements. Besides the depth, the area fraction of the internal attack has also been quantified via binarisation. Fig. 2 (left y-axis) reveals that the highest metal thickness loss is in the coldest zone, samples #8, #9, and #10. While samples at the hottest zone, sample #2 ~ 810 °C, seem to have the lowest metal thickness loss and the shallowest internal attack.

3.2. Results from surface analysis and structural characterisation

Fig. 3 (a) shows selected X-ray diffractograms of alloy 253MA vessel samples exposed to evaporated salt species, while (b) depicts the diffractograms of brushed loose corrosion products from the vessel interior prior to decommission. In Fig. 3(a), signals from the bulk, such as chromium, iron, and nickel, were identified, in addition to magnetite (Fe_3O_4) and iron-chromium oxide $(\text{Cr},\text{Fe})_2\text{O}_3$. Potassium chloride or potassium metal oxide species were detected for all the tested samples. Signals of magnesium chloride and magnesium-containing species were almost absent in the evaporated salt species-environment.

The XRD results of the brushed corrosion products revealed the absence of Mg species in samples located at middle or low-temperature zones, which was also confirmed with EDX point analyses. However, in the hottest zones, samples #2 and #3, Mg ions contributed with 0.2–1.8 at% in the corrosion products in the form of minor cationic fractions of brushed corrosion products.

Due to the complexity of the corroded vessel analysis, Table 3 was designed to summarise our findings regarding the activity or absence of magnesium and potassium species in the corrosion products. In Table 3, the (+) symbol represents the detection of magnesium or potassium salt species, while (–) describes their absence. The number of the (+) sign reflects the intensity of the signal's strength. Therefore, an (+) describes the poor contribution or weak signal of $\text{Mg}^{2+}/\text{K}^+$ in the analysed corrosion products. The results in Table 2 summarise findings in different analytical methods used in this study, i.e., XRD analysis of both vessel specimens and brushed corrosion products. In addition to EDX elemental mapping, point and line-scan analyses.

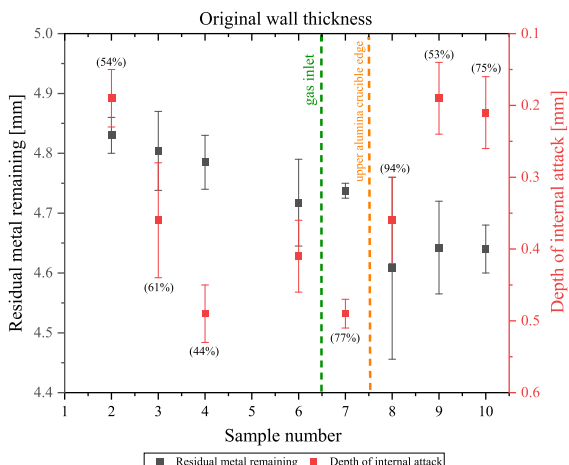


Fig. 2. The left y-axis (in black): Average residual metal wall thickness measured after vessel decommissioning at different heights along the vessel wall. The right y-axis (in red): Average depth of internal attack in the samples. The percentage (%) accompanying the internal attack values represents the measured area fraction of cavities and/or internal oxides. (For interpretation of the references to colour in this figure legend, the reader is referred to the web version of this article.)

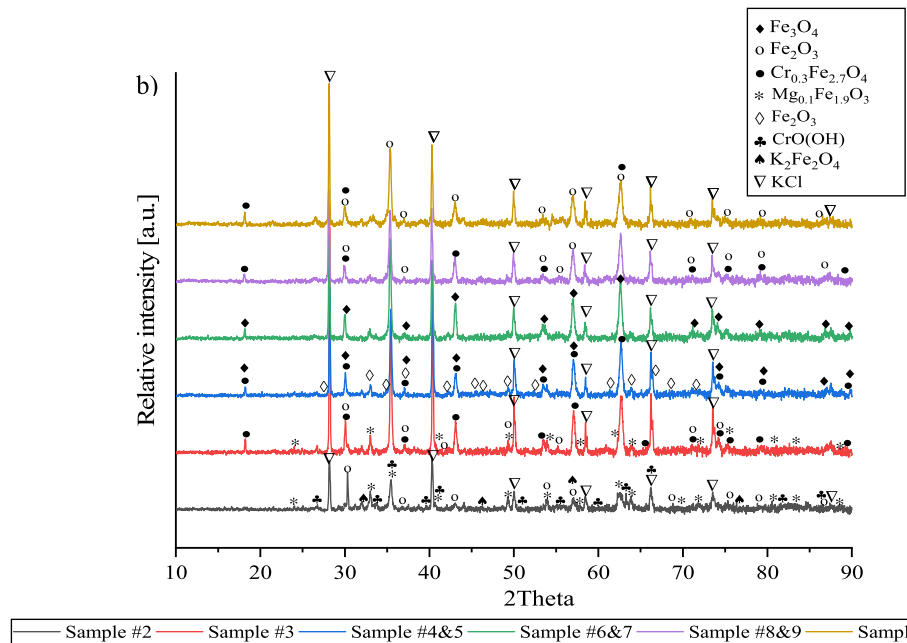
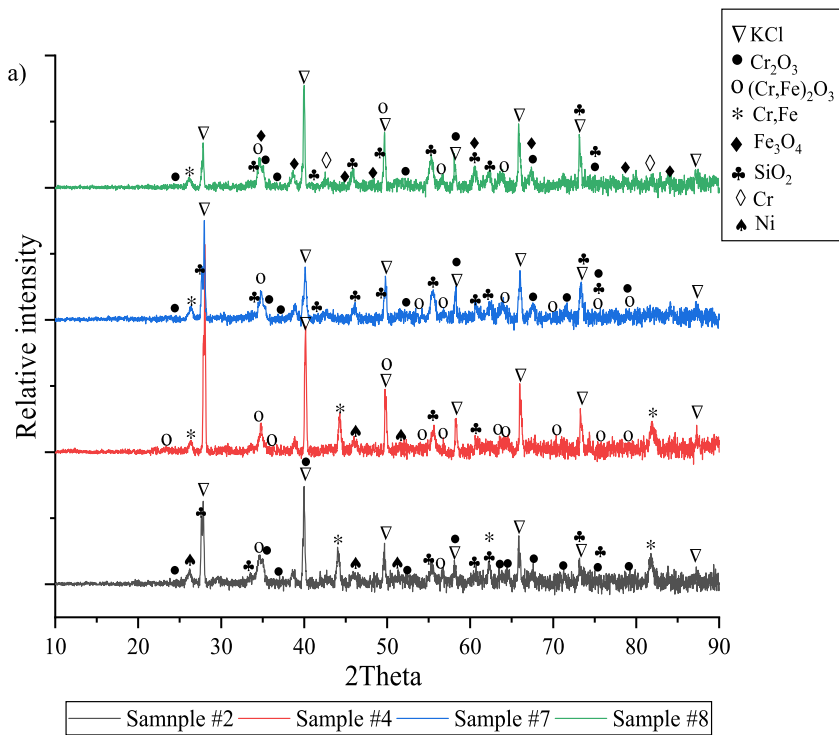


Fig. 3. a) selected XRD diffractograms of vessel samples in positions #2, #4, #7, and #8 exposed to evaporated alkali chloride species after 700 h.
b) XRD diffractograms of brushed corrosion products from 253MA vessel after exposure to evaporated alkali chloride species for 700 h.

3.3. Microscopic inspection of cross-sections

Sections 3.3 (a) and (b) compare the effect of evaporated vs complete immersion of 253MA alloy active in alkali/alkaline earth species.

Table 3

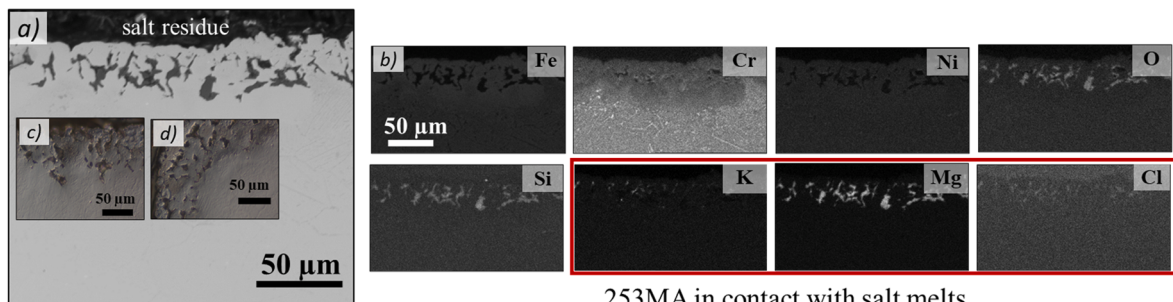
Summary of magnesium and potassium contribution in the investigated corroded vessel using different analytical methods.

Sample no.	Cation species		Internal attack	
	Oxide scale		Mg ²⁺	K ⁺
	Mg ²⁺	K ⁺		
#2	++++	++++	++	++
#3	++++	++++	+	++
#4	-	++++	++	++
#5	-	++++	-	++
#6	-	++++	+	++
#7	-	++++	+	++
#8	++	++++	++	++
#9	+	++++	++	++
#10	-	++++	-	++

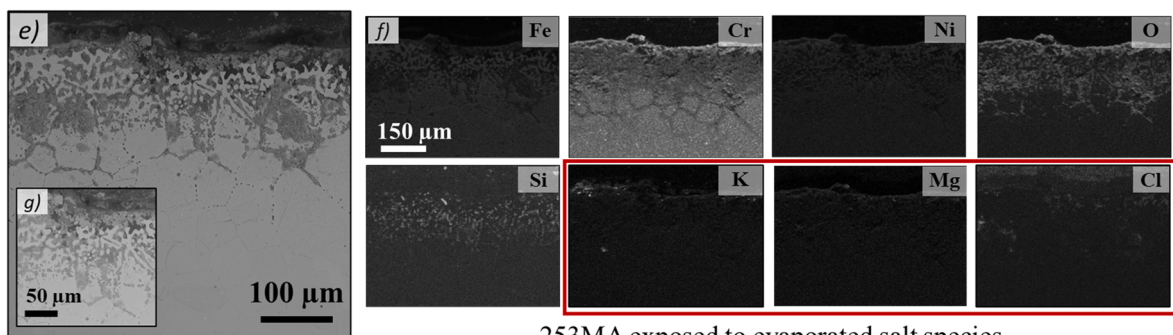
a) Reference - direct contact with the salt melt “immersed”, hottest zone, 800 °C

Fig. 4a depicts the corrosion behaviour of 253MA samples in direct contact with KCl-MgCl₂ melts after ~ 500 h at 800 °C, which serves as a reference for the vessel behaviour. After both 500 h and 700 h exposure to the melt, the cross-section analyses show similar corrosion behaviour identified by an internal attack of the alloy forming cavities partially filled with MgO. These cavities reach 60 ± 20 µm depth into the alloy, which is significantly lower than vessel sample #2 (190 ± 40 µm) exposed to evaporated salt species at the same temperature, see Fig. 4b. The remaining metal thickness was measured to estimate how severe the corrosion attack was; alloy 253MA exposed to evaporated salts species lost 300–500 µm in 700 h, see Fig. 2. In comparison, fully immersed 253MA alloy in melts lost 100–200 µm after 700 h.

Fig. 4b depicts the EDX elemental mapping of a 253MA sample immersed in the binary chloride melt at 800 °C after 500 h. It can be seen that iron and chromium were selectively leached from 50 to 60 µm of the bulk. Chromium was the most depleted element only ~ 3 wt% remaining at 20 µm depth, while nickel was the least leached element. The strong signal of magnesium detected indicates that it was the most active species reacting with the alloy. Weaker signals of potassium have been identified. Overall, the corrosion performance observed is in good agreement with the findings reported in former studies investigating corrosion by chloride melts at high temperatures [10,17,24,39].



253MA in contact with salt melts



253MA exposed to evaporated salt species

Fig. 4. Cross-section SEM image of a 253MA sample immersed in KCl-MgCl₂ melt at 800 °C for ~ 500 h. a) showing cavities formation in bulk. c) EDX elemental mapping showing the most depleted species in the alloy. c,d) cross-section optical microscopy images with a DIC filter of 253MA comparing pores/cavities formation at different sample positions.

b) Indirect contact with the salt melt “evaporation.”

Unlike the corrosion behaviour described in section (a), the evaporated salts species attacked the 253MA vessel differently. In contrast to alloys in direct contact with K^+/Mg^{2+} -chloride melts, magnesium is highly active, forming MgO or an Mg-containing product [17,24,31,40]. None of the 253MA samples along the vessel wall formed a protective oxide scale. Worth reminding that oxygen had access to the vessel wall samples during the vessel opening to pour the melt. In contrast to section (a), oxygen came only from the impurities in the argon gas and humidity in the salts used.

In this section, selected samples along the vessel wall were chosen to present the corrosion attack. The corrosion behaviour is classified according to the temperature gradient across the vessel wall into i) hottest zone, ii) medium-temperature zone, and iii) “coldest” zone; see the temperature gradient in Fig. 1d.

i. Hottest zone ($800 \pm 10^\circ C$)

Key images have been chosen to present the corrosion performance of the 253MA alloy in the hottest zone. Fig. 5 depicts sample #2, $\sim 810^\circ C$, standing without a protective oxide layer against the evaporated salt species. It can be seen that the remaining corrosion products, after brushing the vessel interior, are divided into two zones. In the outer zone at the metal/evaporated salt interface, a cavities network with a worm-like structure is formed with an average thickness of $120 \pm 20 \mu m$. In this zone $\sim 52 \pm 2\%$ of the alloy is oxidised fraction incorporating iron-rich oxides and salt species, particularly KCl and traces of Mg-ions. Beneath this zone, a distinguishable inter-and-intragranular attack occurs, as shown in Fig. 5c, with an oxide/alloy fraction of up to 7%. The intergranular attack consists of internal oxidation along the grain boundaries and selective depletion of alloying elements, as shown in Fig. 5d. In Fig. 5e, Cr seems to be the most depleted element reaching its minimum with less than 2 wt% at the alloy/salt interface, followed by iron, while the nickel fraction seems unaffected.

Finally, $\sim 300 \mu m$ deep into the alloy, only a few intragranular precipitates are present; EDX point analysis shows that these precipitates can be chromium-rich precipitates or chromium-vanadium nitrides. It is also interesting to observe the presence of potassium and chloride species within the attacked grain boundaries. The salt successfully managed to reach $230 \mu m$ deep into the alloy. Samples in positions #3 and #4 showed similar features. However, the worm-like cavities’ network distribution differs along the samples, as indicated by the high “min–max.” range in Fig. 2. In sample #4, the cavities network reaches $\sim 220 \pm 20 \mu m$ deep into the alloy, while in sample #3 is $\sim 120 \pm 20 \mu m$. By contrast, the area fraction of the cavities network in sample #3 is 20% higher than in sample #4.

ii. Medium-temperature zone ($730\text{--}780^\circ C \pm 5^\circ C$)

The corrosion behaviour of samples in the middle-temperature zone (#5, #6 and #7 at $780^\circ C$, $750^\circ C$ and $730^\circ C$, respectively) can

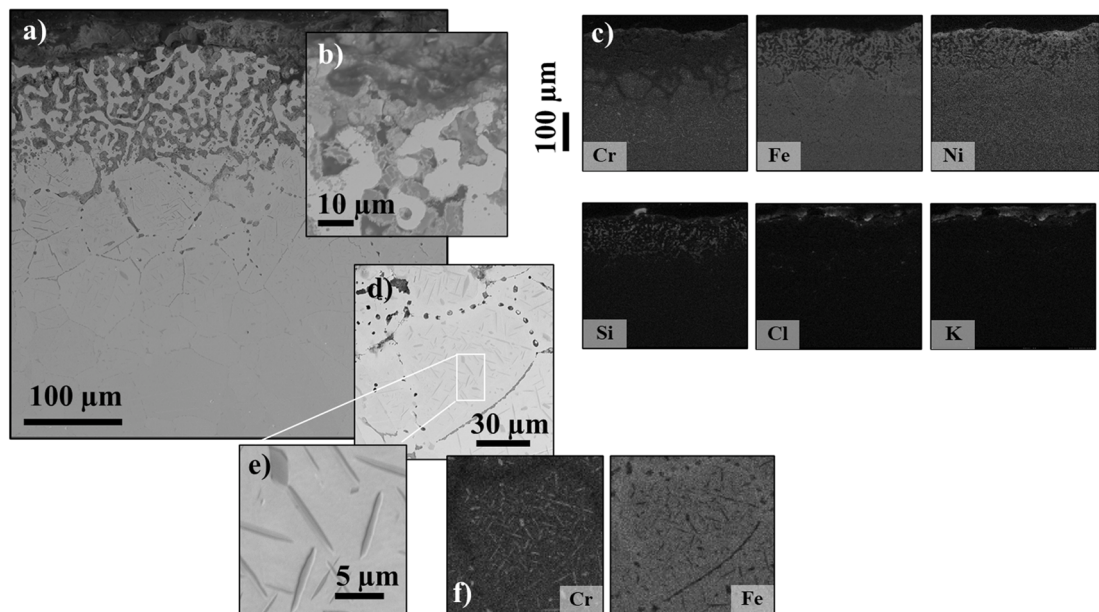


Fig. 5. Cross-section SEM image of sample #2 exposed to evaporated $KCl\text{-}MgCl_2$ melt at $800^\circ C$ for ~ 700 h. a) cavities network reaching hundreds of micrometres deep into the alloy. b) High magnification of image (a) showing pores/cavities filled with salts or internally oxidised. c) EDX elemental mapping showing the most depleted species in the alloy. d) Close-up image of an attacked grain boundary. e) Higher magnification of intra-granular precipitates. f) EDX elemental mapping of image d showing redistribution of alloy elements within the grain boundary.

be described in four main zones: i) outwards growing oxide, ii) cavities/internal oxidation network, iii) horizontal crack, iv) inter and intra-granular attack. Samples in the middle-temperature zone showed an interesting new feature: spallation of the corroded region, as depicted in Figs. 6 and 7. This evident spallation gives an insight into how the corrosion of the 25MA alloy propagates upon salt attack. This zone is also closest to the melt, considering the open alumina crucible position in the vessel (see Fig. 1). As confirmed with the XRD analysis, potassium chloride is deposited at high concentrations at the corrosion front. Interestingly, the magnesium signal was not detected, indicating its absent corrosion activity, unlike what has been observed in direct contact with the melts where Mg^{2+} was the most active species, then K^+ came next.

The EDX elemental mappings in Fig. 6c clearly show chromium depletion from the alloy. Line scans and EDX mapping in Fig. 6d show the inwards diffusion of chromium from the grain boundaries to form the chromium-rich precipitates that have been highlighted earlier.

Since analysing crack fillings was challenging, optical microscopy with a DIC filter was employed to inspect selected samples. Fig. 7a shows a several 100 μm thick salt filling in a horizontal crack completely embedded in the outer corrosion zone which is in the process to propagate and spall. In comparison, Fig. 7b shows a panorama image of horizontal crack propagation at sample #6, where the corroded region above the crack spalls. The observed corroded zone spallation can explain the differences in the remaining metal measured across the vessel walls, as described in Fig. 2a, considering the high amounts of salt precipitation and simultaneous oxidation.

iii. “coldest” zone ($560\text{--}680 \pm 5^\circ C$)

Samples in the coldest zone at positions #8, #9, and #10, with temperatures $680^\circ C$, $630^\circ C$ and $560^\circ C$, respectively, recorded the highest metal thickness loss and the most profound internal attack. Fig. 8 presents key images of the corrosion attack in sample #9 ($630^\circ C$), where (a) shows an internal attack in the form of internal oxidation of cavities filled with salts. The internal attack in the coldest zone reached its highest value in sample #8 ($680^\circ C$) with $580 \pm 80 \mu m$ depth, followed by sample #9 with $350 \pm 40 \mu m$. Lastly, sample #10 ($560^\circ C$) had the shallowest internal attack, recording $210 \pm 50 \mu m$. Interestingly, area fractions of cavities in each zone differ significantly. Comparing cavities in sample #9, it occupies $55 \pm 2\%$ of zone A, $80 \pm 2\%$ of zone B, and $25 \pm 3\%$ in zone C.

EDX point analysis, in agreement with XRD results, shows mainly the formation of iron oxides, iron-chromium oxides, and KCl.

4. Discussion

There was no surprise that 253MA corroded severely when exposed to evaporated alkali/alkaline earth salt species at the operating temperature range used in this study. As discussed earlier, several studies have reported that humidity has the highest potential of initiating and accelerating corrosion in such an environment [5,9,14,35–37]. Spallation, pores formation and non-protective scales have been characterised, in addition to excess leaching of alloy elements from the bulk. However, it was interesting to find that the evaporated alkali species caused more severe damage to the vessel material than direct contact with the melt.

Similar to our findings in a former publication, evaporated alkali carbonate species attacked the hosting vessels severely. The strongest attack did not occur in the hottest zones but in zones exposed most to evaporated salt species [34]. In this study, the most vigorous attack co-relates to zones with higher exposure to evaporated salt species and the highest oxygen impurity level. In other

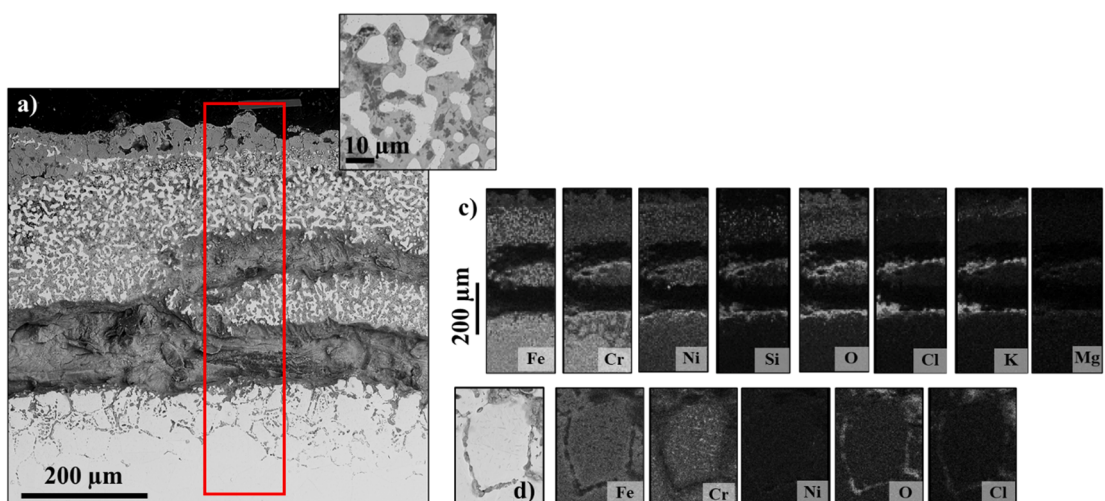


Fig. 6. Cross-section SEM image of sample #7 exposed to evaporated $KCl\text{-}MgCl_2$ melt at $\sim 730^\circ C$ for ~ 700 h showing four distinct corrosion zones. b) High magnification of image (a) showing pores/cavities filled with salts or internally oxidised. c) EDX elemental mapping showing the most depleted and active species in the tested section. d) Higher magnification of an attacked grain boundary describing the inter- and intra-granular precipitates.

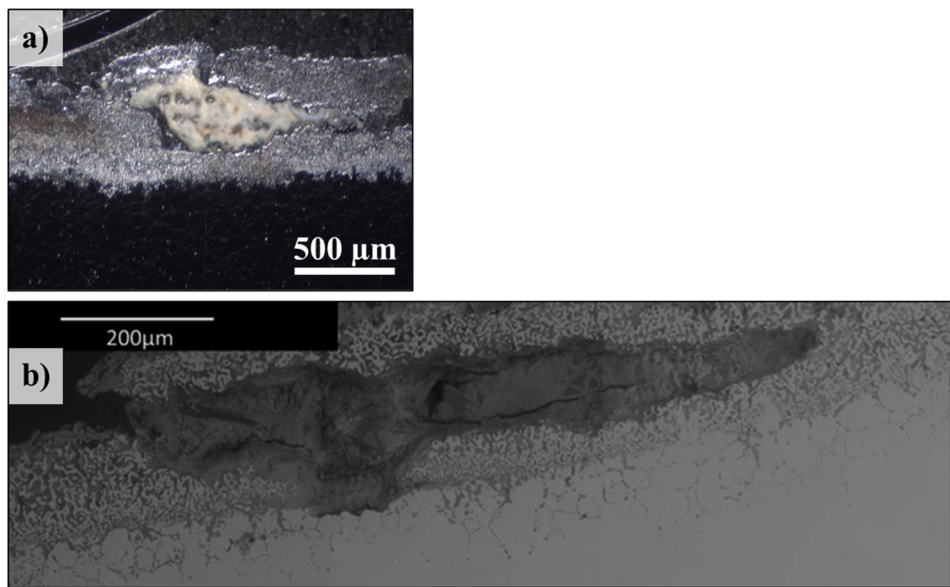


Fig. 7. a) an optical microscopy image with DIC filter, b) an SEM panorama image Cross-section of sample #6 exposed to evaporated KCl-MgCl₂ melt at ~ 750 °C for ~ 700 h showing a horizontal crack filled with trapped salts before it spalls off.

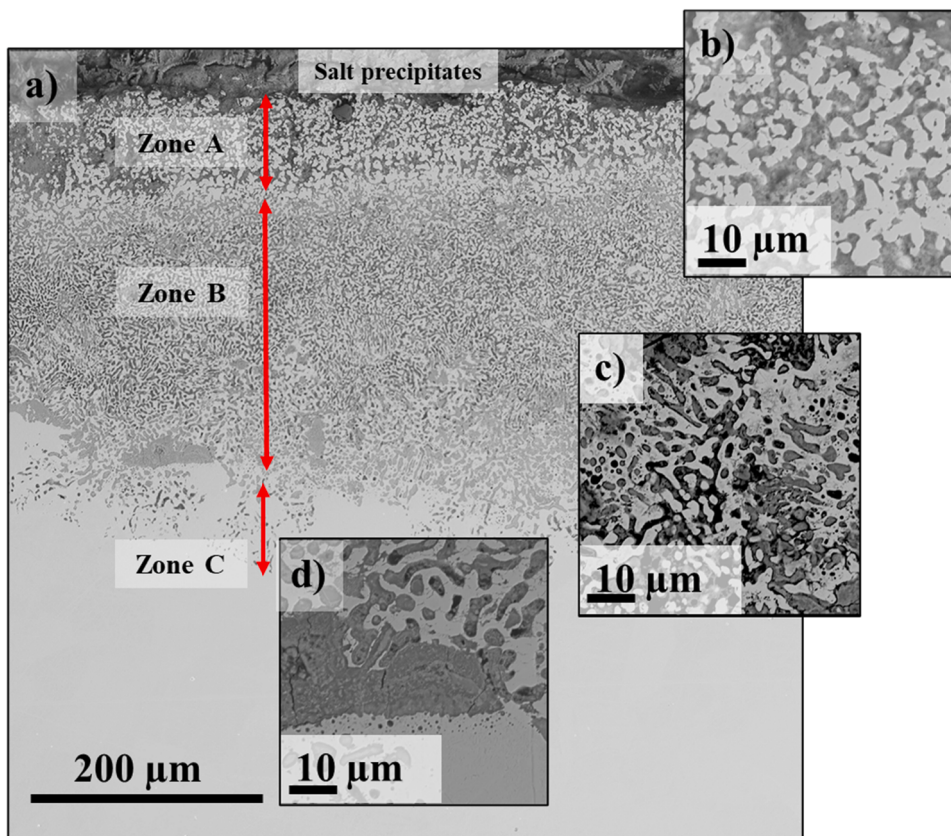


Fig. 8. a) Cross-section SEM image of sample #9 exposed to evaporated KCl-MgCl₂ melt at ~ 750 °C for ~ 700 h showing three distinguishable corrosion zones. b, c, and d) High magnification images for features in each corrosion zone.

words, vessel sections close to the lid, experiencing salt condensation and higher pO_2 during vessel openings, are expected to have higher corrosion attacks than other sections. In addition, as described in 2.4, the evaporation of salts and their condensation on the vessel lid clogged occasionally the Ar gas exhaust line. The outlet line clogging was observed after 96 h preventing Ar gas from sweeping away corrosion products formed by $MgCl_2$ hydrolysis and other volatile corrosion products. Using the built-in metal rod to clean the exhaust line frequently, volatile species were swept away regularly. However, one needs to consider that the concentration of these species can increase during exposure, accelerating the corrosion rate. In addition to pushing evaporated clogging salt species deep into the vessel during the exhaust-line cleaning step.

As discussed in 3.1, different parameters need to be considered for evaluating corrosion behaviour along the vessel. Despite the remaining metal thickness seeming to give reliable data on how much metal was lost, one needs to consider the internal oxidation depth. Also, we need to consider the percentage of cavities area fraction for a better evaluation.

Based on our experimental results, one can describe the corrosion processes in 253MA alloy exposed to evaporated salt species into four main phenomena. The corrosion processes could be described as i) formation of non-protective outwards growing Fe-rich oxide, ii) metal leaching from the bulk, leaving cavities behind, iii) spallation of the corroded region, and finally, 4) inter and intra-granular attack and precipitates formation. A schematic illustration in Fig. 9 depicts a possible corrosion mechanism of a metallic material in contact with KCl and oxygen inspired by Cantatore et al. [41]. In the same publication, the impact of water is also depicted, which has not been shown here. The alloy can form a metal oxide at the metal/gas interface in the presence of oxygen. The oxide scale growth occurs via inward diffusion of oxyanion (O^{2-}). Folkeson et al. anticipated steel chlorination by KCl in the presence of oxygen, where chloride ions can diffuse through the formed oxide scale [42,43]. Building on Folkeson et al. assumption, Cantatore et al. proposed that chloride ion diffusion would follow the anion vacancies along the oxide scale, which form upon oxide scale growth [41].

All the transients of potassium metalates ($K_aM_bO_c$) and oxychlorides ($M_xO_yCl_z$) are associated with the porosity detected.

Another feature that has been observed is the inter-and intra-granular precipitates in connection with the alloy/oxide interface. Since these precipitates were only observed upon exposure to evaporated salt species and not detected in sections close to the air side, we believe these precipitates were triggered by chromium leaching where alloy equilibrium shifted towards precipitates; see Fig. 5(e).

What was surprising was the absence of Mg-containing species; only potassium-containing corrosion products were detected with XRD and EDX analyses, which contradicts findings that small cations are the most aggressive [4,31]. Mohan et al. used FactSage to predict the vapour pressure of NaCl, KCl, $MgCl_2$ and three mixtures of these three salts. In their study, KCl, $MgCl_2$, and K/Mg-chloride mixture have an almost similar vapour pressure in the temperature range of 550–700 °C. At temperatures higher than 700 °C, $MgCl_2$ had the highest vapour pressure, and then KCl and K/Mg-chloride mixture came last [38]. Despite the previously mentioned studies, Mg-ions and salt species were almost exclusively noted in corrosion products caused by full immersion in small amounts in the hottest vessel section, samples #2 and #3, at ~800 °C ± 10 °C.

It is noteworthy to remind the reader that the binary salt mixture used in this study contains a 2:1 mass ratio of KCl/ $MgCl_2$.

Based on our experimental observations, evaporated KCl is enriched within horizontal cracks. As discussed earlier, KCl can react with chromia in the presence of oxygen and forms K_2CrO_4 (I). In the presence of oxygen, excessive chromium leaching occurs, preferably along grain boundaries, which can explain the intergranular attack seen in Section 3.3.

As described in Section 2.2 at 800 °C, the 253MA mass fraction of the FCC phase is expected to be reduced from being almost only phase to 92.14%, and fractions of $(Cr,V)_2N$, $M_{23}C_6$, $(Cr,Fe)_3P$, Ce_2S_3 , η -phase and σ -phase precipitates. It is important to highlight that these calculations are made upon a change in temperature from 1050 °C to 800 °C without investigating the salt species effect. Despite the intra-granular precipitates being observed, Fig. 5 d–f, these precipitates were only detectable on the vessel sections exposed to evaporated salt, not the air side. This means that the aforementioned precipitates are triggered by salt's attack and formed upon metals leaching.

As described in the introduction, anodic protection against molten chloride attack by Mg addition into the melt does not protect materials from evaporated species. Thus, it is advisable to avoid space gas phases in thermal storages or heat transfer medium pipes at high temperatures.

5. Conclusions

In this study, corrosion damages caused by the K/Mg-eutectic chloride melt and their impurities in contact with metals have been evaluated as well as the impact of evaporating species and their difference in corrosivity.

With this article, we want to point out three differences for consideration:

- The molar fraction of gaseous impurities mixed with evaporating salt species is substantially higher than in the melt itself. The highest corrosion attack is independent of the temperature gradient. Instead, the vigorous attack occurs at zones exposed to the highest evaporated salt species concentration and oxygen impurity level.
- The damage of the 253MA caused by evaporated salt species was significantly more-severe compared to fully immersed 253MA samples in $MgCl_2$ -KCl melt. The estimated metal thickness losses, extrapolated linearly for one year, for the 253MA alloy at 800 °C fully immersed in $MgCl_2$ -KCl melt is ~0.8 mm/year compared to ~2.1 mm/year when exposed to evaporated salt species. In comparison, sample #8 (680 °C) at the coldest zone is expected to witness a thickness mass loss of ~5.0 mm/year by applying linear extrapolation.
- The most active alkali chloride species in the corrosion products found along the vessel wall has been potassium chloride, in strong contrast to the dominating role of magnesium ions found in internal corrosion products of samples fully immersed in the chloride melt.

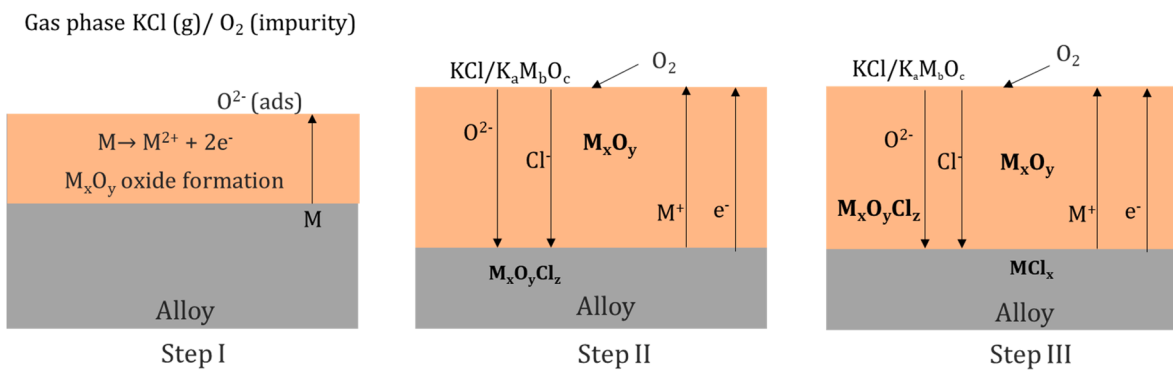


Fig. 9. A schematic illustrates the proposed corrosion mechanism for alloys in contact with KCl and O₂. Inspired by the work conducted by Cantatore et al. [41].

- Consequently, the addition of metallic magnesium as a corrosion inhibitor will be active for the metal in direct contact with the melt, as proven in several studies discussed earlier in the introduction. However, alloy components exposed to gaseous species above the melt do not necessarily benefit since the inhibitor cannot reach these areas to inactivate cover gas impurities.

Declaration of Competing Interest

The authors declare that they have no known competing financial interests or personal relationships that could have appeared to influence the work reported in this paper.

Data availability

Data will be made available on request.

Acknowledgements

This work has been financially supported by the Research and Research Education Committee at Chemistry and Chemical Engineering Department, Chalmers University of Technology. Part of the work has received funding from High-Temperature Corrosion (HTC) Centre via Swedish Energy Agency within the thermal storage for SOLEL initiative under contract number 44653-1 (2017–2021).

References

- M. Mehos et al., Concentrating Solar Power Gen3 Demonstration Roadmap, National Renewable Energy Lab. (NREL), NREL/TP-5500-67464 United States 10.2172/1338899 NREL English, 2017. [Online]. Available: <https://www.osti.gov/servlets/purl/1338899>.
- J.C. Gomez-Vidal, R. Tirawat, Corrosion of alloys in a chloride molten salt (NaCl-LiCl) for solar thermal technologies, *Sol. Energy Mater. Sol. Cells* 157 (2016/12/01/2016,) 234–244, <https://doi.org/10.1016/j.solmat.2016.05.052>.
- W. Ding, A. Bonk, J. Gussoni, T. Bauer, Electrochemical measurement of corrosive impurities in molten chlorides for thermal energy storage, *J. Storage Mater.* 15 (2018/02/01/ 2018,) 408–414, <https://doi.org/10.1016/j.est.2017.12.007>.
- A. Rahmel, in: *Corrosion*, Springer, US, Boston, MA, 1982, pp. 265–283.
- W. Ding, T. Bauer, Progress in research and development of molten chloride salt technology for next generation concentrated solar power plants, *Engineering* 7 (3) (2021) 334–347, <https://doi.org/10.1016/j.eng.2020.06.027>.
- A.M. Kruizinga, Corrosion mechanisms in chloride and carbonate salts, Sandia National Laboratories (SNL), Albuquerque, NM, and Livermore, CA (United States), 2012.
- I.N. Ozeryanaya, Corrosion of metals by molten salts in heat-treatment processes, *Met. Sci. Heat Treat.* 27 (3) (1985/03/01 1985,) 184–188, <https://doi.org/10.1007/BF00699649>.
- Y.S. Li, M. Spiegel, Models describing the degradation of FeAl and NiAl alloys induced by ZnCl₂-KCl melt at 400–450 °C, *Corros. Sci.* 46 (8) (2004/08/01/2004,) 2009–2023, <https://doi.org/10.1016/j.corsci.2003.10.019>.
- Z. Ge, Y. Huang, Y. Ding, Eutectic composition-dependence of latent heat of binary carbonates (Na₂CO₃/Li₂CO₃), *Sol. Energy Mater. Sol. Cells* 179 (2018/06/01/2018,) 202–206, <https://doi.org/10.1016/j.solmat.2017.11.015>.
- W. Ding et al., Hot corrosion behavior of commercial alloys in thermal energy storage material of molten MgCl₂/KCl/NaCl under inert atmosphere, in: *Solar Energy Materials and Solar Cells* vol. 184, ed: Elsevier B.V., 2018, pp. 22–30.
- Y. Zhao, J. Vidal, Potential scalability of a cost-effective purification method for MgCl₂-Containing salts for next-generation concentrating solar power technologies, *Sol. Energy Mater. Sol. Cells* 215 (2020), <https://doi.org/10.1016/j.solmat.2020.110663>.
- W. Ding, J. Gomez-Vidal, A. Bonk, T. Bauer, Molten chloride salts for next generation CSP plants: Electrolytical salt purification for reducing corrosive impurity level, *Sol. Energy Mater. Sol. Cells* 199 (2019/09/01/ 2019,) 8–15, <https://doi.org/10.1016/j.solmat.2019.04.021>.
- A.G. Fernández, L.F. Cabeza, Corrosion evaluation of eutectic chloride molten salt for new generation of CSP plants. Part 1: Thermal treatment assessment, in: *Journal of Energy Storage* vol. 27, ed: Elsevier, 2020, p. 101125.
- J. M. Kurley, P. W. Halstenberg, A. McAlister, S. Rainman, S. Dai, R.T. Mayes, Enabling chloride salts for thermal energy storage: implications of salt purity, *RSC Adv.*, 10.1039/C9RA03133B vol. 9, no. 44, pp. 25602–25608, 2019, doi: <https://doi.org/10.1039/C9RA03133B>.
- H. Li, X. Yang, X. Yin, X. Wang, J. Tang, J. Gong, Effect of Chloride Impurity on Corrosion Kinetics of Stainless Steels in Molten Solar Salt for CSP Application: Experiments and Modeling, *Oxid. Met.* 95 (3) (2021/04/01 2021,) 311–332, <https://doi.org/10.1007/s11085-021-10025-y>.

- [16] G.J. Kipouros, D.R. Sadoway, A thermochemical analysis of the production of anhydrous MgCl₂, *J. Light Met.* 1 (2) (2001/05/01/ 2001,) 111–117, [https://doi.org/10.1016/S1471-5317\(01\)00004-9](https://doi.org/10.1016/S1471-5317(01)00004-9).
- [17] B. Liu, X. Wei, W. Wang, J. Lu, J. Ding, Corrosion behavior of Ni-based alloys in molten NaCl-CaCl₂-MgCl₂ eutectic salt for concentrating solar power, *Sol. Energy Mater. Sol. Cells* 170 (2017/10/01/ 2017,) 77–86, <https://doi.org/10.1016/j.solmat.2017.05.050>.
- [18] K. Vignaraooban, P. Pugazhendhi, C. Tucker, D. Gervasio, A.M. Kannan, Corrosion resistance of Hastelloys in molten metal-chloride heat-transfer fluids for concentrating solar power applications, *Sol. Energy* 103 (2014/05/01/ 2014,) 62–69, <https://doi.org/10.1016/j.solener.2014.02.002>.
- [19] K. Vignaraooban et al., Vapor pressure and corrosivity of ternary metal-chloride molten-salt based heat transfer fluids for use in concentrating solar power systems, in: *Applied Energy* vol. 159, ed, 2015, pp. 206–213.
- [20] F. Mansfeld, N.E. Paton, W.M. Robertson, The high temperature behavior of superalloys exposed to sodium chloride: II. corrosion, *Metall. Trans. A* 4 (1) (1973/01/01 1973,) 321–327, <https://doi.org/10.1007/BF02649632>.
- [21] R. Pillai, S.S. Raiman, B.A. Pint, First steps toward predicting corrosion behavior of structural materials in molten salts, *J. Nucl. Mater.* 546 (2021/04/01/ 2021,) 152755, <https://doi.org/10.1016/j.jnucmat.2020.152755>.
- [22] N.S. Patel, V. Pavlík, M. Boča, High-Temperature Corrosion Behavior of Superalloys in Molten Salts—A Review, in: *Critical Reviews in Solid State and Materials Sciences* vol. 42, ed: Taylor & Francis, 2017, pp. 83–97.
- [23] W. Ding, A. Bonk, T. Bauer, Corrosion behavior of metallic alloys in molten chloride salts for thermal energy storage in concentrated solar power plants: A review, *Front. Chem. Eng.* 12 (3) (2018/09/01 2018,) 564–576, <https://doi.org/10.1007/s11705-018-1720-0>.
- [24] J.C. Gomez-Vidal, A.G. Fernandez, R. Tirawat, C. Turchi, W. Huddleston, Corrosion resistance of alumina forming alloys against molten chlorides for energy production. II: Electrochemical impedance spectroscopy under thermal cycling conditions, in: *Solar Energy Materials and Solar Cells* vol. 166, ed: Elsevier B.V., 2017, pp. 234–245.
- [25] D.L. Maricle, D.N. Hume, A new method for preparing hydroxide-free alkali chloride melts, *Massachusetts Inst. of Tech., Cambridge. Lab. for Nuclear Science, United States*, 1959-01-01 1959, [Online]. Available: <https://www.osti.gov/biblio/4197980>.
- [26] A. Mortazavi, Y. Zhao, M. Esmaily, A. Allanore, J. Vidal, N. Birbilis, High-temperature corrosion of a nickel-based alloy in a molten chloride environment – The effect of thermal and chemical purifications, *Sol. Energy Mater. Sol. Cells* 236 (2022/03/01/ 2022,) 111542, <https://doi.org/10.1016/j.solmat.2021.111542>.
- [27] N. Klammer, C. Engrakul, Y. Zhao, Y. Wu, J. Vidal, Method To Determine MgO and MgOCl in Chloride Molten Salts, *Anal. Chem.* 92 (5) (2020/03/03 2020,) 3598–3604, <https://doi.org/10.1021/acs.analchem.9b04301>.
- [28] A.G. Fernández, L.F. Cabeza, Anodic Protection Assessment Using Alumina-Forming Alloys in Chloride Molten Salt for CSP Plants, *Coatings* 10 (2) (2020) pp, <https://doi.org/10.3390/coatings10020138>.
- [29] W. Ding, et al., Molten chloride salts for next generation concentrated solar power plants: Mitigation strategies against corrosion of structural materials, *Sol. Energy Mater. Sol. Cells* 193 (2019/05/01/ 2019,) 298–313, <https://doi.org/10.1016/j.solmat.2018.12.020>.
- [30] J.R. Keiser, J.H. DeVan, E.J. Lawrence, Compatibility of molten salts with type 316 stainless steel and lithium, *J. Nucl. Mater.* vol. 85–86 (1979/12/02/ 1979,) 295–298, [https://doi.org/10.1016/0022-3115\(79\)90505-1](https://doi.org/10.1016/0022-3115(79)90505-1).
- [31] E. Hamdy, J. Nockert-Olovjö, C. Geers, Perspectives on selected alloys in contact with eutectic melts for thermal storage: Nitrates, carbonates and chlorides, *Sol. Energy* 224 (2021/08/01/ 2021,) 1210–1221, <https://doi.org/10.1016/j.solener.2021.06.069>.
- [32] E. Hamdy, J. Nockert-Olovjö, C. Geers, Additional data and experimental setups used for the study on alloys in contact to high temperature eutectic melts for thermal storage, *Data Brief* (2021), 107446, <https://doi.org/10.1016/j.dib.2021.107446>.
- [33] E. Hamdy, M. Strach, J. Nockert-Olovjö, C. Geers, Differentiation in corrosion performance of alumina forming alloys in alkali carbonate melts, *Corros. Sci.* (2021/09/20/ 2021,) 109857, <https://doi.org/10.1016/j.corsci.2021.109857>.
- [34] E. Hamdy, A. Wagné, C. Geers, Evaporated Alkali Carbonate Effect on an Aluminum Diffusion Coated 253MA Vessel after 4000 h Discontinuous Operation—Lessons Learned, *Energies* 15 (9) (2022) 3241, <https://doi.org/10.3390/en15093241>.
- [35] Y. Tian, C.Y. Zhao, A review of solar collectors and thermal energy storage in solar thermal applications, *Appl. Energy* 104 (2013/04/01/ 2013,) 538–553, <https://doi.org/10.1016/j.apenergy.2012.11.051>.
- [36] H.R. Copson, Corrosion of Heating Electrodes in Molten Chloride Baths, *J. Electrochem. Soc.* 100 (6) (1953) 257, <https://doi.org/10.1149/1.2781115>.
- [37] W. Ding, A. Bonk, T. Bauer, Molten chloride salts for next generation CSP plants: Selection of promising chloride salts & study on corrosion of alloys in molten chloride salts, in: AIP conference proceedings, vol. 2126, no. 1, AIP Publishing LLC, 2019, p. 200014, <https://doi.org/10.1063/1.5117729>.
- [38] G. Mohan, M. Venkataraman, J. Gomez-Vidal, J. Coventry, Assessment of a novel ternary eutectic chloride salt for next generation high-temperature sensible heat storage, *Energ. Convers. Manage.* 167 (2018/07/01/ 2018,) 156–164, <https://doi.org/10.1016/j.enconman.2018.04.100>.
- [39] Y. Hu, Y. Qin, H. Zhou, Corrosion behavior of NO6600 alloy in molten chloride salts, in: IOP Conference Series: Materials Science and Engineering vol. 394, ed, 2018.
- [40] W.J. Ding, J. Gomez-Vidal, A. Bonk, T. Bauer, Molten chloride salts for next generation CSP plants: Electrolytical salt purification for reducing corrosive impurity level, *Sol. Energy Mater. Sol. Cells* 199 (Sep 2019) 8–15, <https://doi.org/10.1016/j.solmat.2019.04.021>.
- [41] V. Cantatore, et al., Oxidation Driven Permeation of Iron Oxide Scales by Chloride from Experiment Guided First-Principles Modeling, *J. Phys. Chem. C* 123 (42) (2019/10/24 2019,) 25957–25966, <https://doi.org/10.1021/acs.jpcc.9b06497>.
- [42] N. Folkeson, L.-G. Johansson, J.-E. Svensson, Initial stages of the HCl-induced high-temperature corrosion of alloy 310, *J. Electrochem. Soc.* 154 (9) (2007) C515.
- [43] N. Folkeson, T. Jonsson, M. Halvarsson, L.G. Johansson, J.E. Svensson, The influence of small amounts of KCl (s) on the high temperature corrosion of a Fe-2.25 Cr-1Mo steel at 400 and 500° C, *Mater. Corros.* 62 (7) (2011) 606–615.